Journal of Geophysical Research: Space Physics

RESEARCH ARTICLE
10.1029/2018JA025933

GPS Scintillations and Losses of Signal Lock at High Latitudes During the 2015 St. Patrick's Day Storm

Yaqi Jin[1] and **Kjellmar Oksavik**[2,3]

[1]Department of Physics, University of Oslo, Oslo, Norway, [2]Birkeland Centre for Space Science, Department of Physics and Technology, University of Bergen, Bergen, Norway, [3]Arctic Geophysics, University Centre in Svalbard, Longyearbyen, Norway

Key Points:
- Significant GPS amplitude and phase scintillations were observed in association with a TEC blob in the polar ionosphere
- The geomagnetic storm resulted in losses of lock in the GPS L2 band and a 12-dB-Hz signal power drop in the L1 band
- Ionospheric irregularities cause signal power fades and rapid phase fluctuations, which both contribute to losses of lock for GPS signals

Supporting Information:
- Supporting Information S1
- Figure S1

Correspondence to:
Y. Jin,
yaqi.jin@fys.uio.no

Citation:
Jin, Y., & Oksavik, K. (2018). GPS scintillations and losses of signal lock at high latitudes during the 2015 St. Patrick's Day storm. *Journal of Geophysical Research: Space Physics*, *123*, 7943–7957. https://doi.org/10.1029/2018JA025933

Received 24 JUL 2018
Accepted 31 AUG 2018
Accepted article online 5 SEP 2018
Published online 26 SEP 2018

Abstract We investigate the Global Positioning System (GPS) amplitude and phase scintillations during a severe geomagnetic storm on 17 March 2015. The auroral oval expanded significantly due to a strongly southward interplanetary magnetic field (B_z was −25 nT). When the auroral oval was over Skibotn in northern Norway, significant enhancements in total electron content (TEC) fluctuations, amplitude, and phase scintillation were observed. The strongest amplitude and phase scintillations were observed when a TEC blob propagated across the field of view. Strong amplitude and phase scintillations were observed near the edges of the TEC blob. The European Incoherent SCATter ultrahigh frequency radar observed significant enhancement of electron density (from 0.8×10^{11} to 1.6×10^{11} m^{-3}) near the edge of the TEC blob in the F_2 region, while the E region was only slightly enhanced. This indicates that the plasma processes and instability modes, which accounted for the strong GPS scintillations, should involve the F_2 region ionosphere. We also analyzed the tracking performance of the GPS receiver during strong ionospheric scintillation condition. While the receiver maintained tracking of the GPS L1 signal, the strong amplitude scintillation resulted in a power fade up to 12 dB-Hz. Losses of lock occurred in the GPS L2 band. Both the power fade and rapid phase fluctuation should contribute to losses of lock.

Plain Language Summary We study the disturbance of satellite navigation signals (Global Navigation Satellite Systems, GNSS) during a severe geomagnetic storm on 17 March 2015. Substantial changes in the ionosphere caused degraded performance of the GNSS service through degrading the signal quality and/or failed signal tracking. The study of the GNSS receiver tracking performance under strong ionospheric scintillations provides important guidelines for future research and development of mitigation techniques.

1. Introduction

As our modern society relies more and more on Global Navigation Satellite Systems (GNSS) technology in positioning and precise timing, any extended disruption of the GNSS service will affect our daily life. However, the performance of GNSS services is highly dependent on processes in the ionosphere. When the GNSS signal passes through regions of ionospheric irregularities, the ionospheric scintillation occurs due to the interference of the radio waves. Consequently, the signal that has traversed the ionosphere exhibits rapid fluctuations in amplitude and phase, which are referred to as amplitude and phase scintillations, respectively (see, e.g., Yeh & Liu, 1982; Kintner et al., 2007, and references therein). The signal quality is degraded during intense scintillations, and the GNSS receiver may not be able to maintain lock of the signal. In this case, the GNSS service may become unavailable.

At high latitudes, the scintillation effect on Global Positioning System (GPS) signals has been associated with phenomena like storm-enhanced density, polar cap patches, and auroral precipitation (Alfonsi et al., 2011; De Franceschi et al., 2008; Jin et al., 2014, 2015; Jin, Moen, et al., 2016; Li et al., 2010; Mitchell et al., 2005; Moen et al., 2013; Oksavik et al., 2015; Prikryl et al., 2010, 2011, 2013; Smith et al., 2008; Spogli et al., 2009; van der Meeren et al., 2014, 2015, 2016). The strongest GPS phase scintillations are associated with auroral blobs that are formed when polar cap patches enter the nightside auroral region (Jin et al., 2014; Jin, Moen, et al., 2016; van der Meeren et al., 2015). Similar results have been reported in the dayside cusp ionosphere, where the polar cap patches combined with the cusp auroral dynamics are associated with the strongest GPS phase scintillation (Jin et al., 2015, 2017; Oksavik et al., 2015).

The GNSS service can be particularly disturbed during severe geomagnetic storms which are driven by the interplanetary coronal mass ejections (ICMEs) or corotating interaction regions (e.g., Prikryl et al., 2014). In this paper we now investigate one of the largest geomagnetic storms during the last solar maximum, the St. Patrick's Day storm on 17 March 2015. Most studies have focused on geomagnetic conditions that are far less active and mostly report phase scintillations of GPS signals at high latitudes. However, extreme events like the St. Patrick's Day storm are likely candidates for even stronger disruptions. In the current study we report significant amplitude scintillation of GPS signals at high latitudes as well, in addition to phase scintillation. We also quantify the signal power drop and loss of signal lock during the St. Patrick's Day storm. Finally, we relate the disruptions to large-scale phenomena like total electron content (TEC) blobs.

2. Instrumentation

The essential data set for the current study is the GPS TEC and scintillation data at Skibotn in northern Norway (69.43°N, 20.38°E; 66.28°N magnetic latitude [MLAT]). This receiver is the standard GPS Ionospheric Scintillation/TEC Monitor, model GSV4004 (Van Dierendonck et al., 1993). The amplitude (S_4) and phase (σ_ϕ) scintillation indices at the GPS L1 band (1.5754 GHz) are calculated and recorded automatically by the GPS Ionospheric Scintillation/TEC Monitor. The phase scintillation index (σ_ϕ) is defined as the standard deviation of the carrier phase that has been detrended by a high-pass sixth-order Butterworth filter with a cutoff frequency of 0.1 Hz:

$$\sigma_\phi = \sqrt{\langle \phi^2 \rangle - \langle \phi \rangle^2}$$

where $\langle . \rangle$ denotes the expected value over 60 s, and ϕ is the detrended carrier phase.

The amplitude scintillation index (S_4) is defined as the ratio of the standard deviation of the signal amplitude to the mean signal amplitude:

$$S_4 = \sqrt{\frac{\langle I^2 \rangle - \langle I \rangle^2}{\langle I \rangle^2}}$$

where $\langle . \rangle$ denotes the expected value over 60 s of the quantity, and I is the amplitude data that are detrended by dividing the raw amplitude (I_{raw}) by the filtered amplitude ($I_{filtered}$) using a low-pass sixth-order Butterworth filter (Van Dierendonck et al., 1993):

$$I = \frac{I_{raw}}{I_{filtered}}$$

The output amplitude and phase scintillation indices from the GPS scintillation receiver are of 60-s resolution.

Besides the phase scintillation indices, we also record the high-resolution raw data (GPS carrier phase and received signal amplitude) at 50 Hz. To show the high-resolution variation of the GPS data, we reprocess the high-resolution raw GPS data and calculate 1-s resolution GPS scintillation indices in the same manner as the 60-s values. In this situation, we detrend the raw GPS carrier phase data by first subtracting a fourth-order polynomial fit from the raw phase and then filtering the result using a high-pass Butterworth filter with a cutoff frequency of 0.3 Hz (e.g., van der Meeren et al., 2014).

The receiver can also calculate and record the GPS TEC data based on 1-s measurements at L1 and L2 frequencies. However, the TEC is not calibrated and contains instrumental biases from the satellite and receiver. We use the GPS-SCINDA software to calibrate the GPS TEC (Carrano et al., 2009). The calibrated GPS TEC data have 60-s resolution. We can also calculate the rate of change of the TEC (ROT), which is a measure of the small-scale variation of the GPS TEC data.

When presenting the scintillation data on top of GPS TEC maps in Figure 6, we also include observations from the GNSS scintillation receivers at Ny-Ålesund (78.9°N, 11.9°E; 76.4°N MLAT), Longyearbyen (78.1°N, 16.0°E; 75.4°N MLAT), Hopen (76.5°N, 25.0°E; 73.3°N MLAT), and Bjørnøya (74.5°N, 19.0°E; 71.6°N MLAT). These four NovAtel GPStation-6 receivers are operated by the University of Bergen since 2013 (Oksavik et al., 2015; van der Meeren et al., 2015), and they can track signals from GPS (L1/L2/L2C/L5), GLObal NAvigation

Satellite System (GLONASS; L1/L2), and Galileo (E1/E5a/E5b/Alt-BOC; Oksavik et al., 2015). In this study, we only use data of the phase scintillation index in the L1 band of GPS and GLONASS in Figure 6.

For global auroral observations, we use data from the Special Sensor Ultraviolet Spectrographic Imager (SSUSI) on board the Defense Meteorological Satellite Program (DMSP) satellites F16–F19. SSUSI makes auroral observations at five wavelengths in the far ultraviolet range (115–180 nm) with high spatial resolution (7–9 km at nadir) by scanning across the track of the DMSP trajectory every 15 s (see, e.g., Paxton et al., 2002). In this study, the emission from N2 Lyman-Birge-Hopfield long filter (LBHL) band (165–180 nm) is used to represent the aurora. The velocity data from the ion drift meter is also used to show the expanded convection cell and enhanced ion velocity (Greenspan et al., 1986).

The European Incoherent SCATter (EISCAT) UHF (ultrahigh frequency) radar in Tromsø, Norway (69.58°N, 19.23°E; 66.73° N MLAT), operated from 10:50 to 13:50 UT. The UHF radar beam was fixed at an azimuthal angle of 185° and elevation angle of 77° (i.e., in the field-aligned direction in the *F* region). The data were post-processed and integrated for 60 s using the GUISDAP analysis toolbox (http://www.eiscat.com/groups/Documentation/UserGuides/GUISDAP/; Huuskonen & Lehtinen, 1996).

In addition, we also use the OMNI solar wind data, auroral electrojet (*AE*), and *Sym-H* indices. We use the interplanetary magnetic field (IMF) data in geocentric solar magnetospheric coordinates from the 1-min resolution OMNI data set (King & Papitashvili, 2005). The OMNI IMF data are already shifted from the observation points to the Earth's bow shock nose. We use the 1-min resolution *Sym-H* and *AE* indices to show the geomagnetic storm and substorm activity. The *Sym-H* and *AE* indices were obtained from the World Data Center for Geomagnetism at Kyoto University (http://wdc.kugi.kyoto-u.ac.jp/).

3. Observation

Figures 1a–1d give an overview of the geomagnetic storm and the global response in terms of geomagnetic indices. The geomagnetic storm was driven by an ICME from the Sun (Kamide & Kusano, 2015; Kataoka et al., 2015). It involved a two-step development, driven by the two successive intervals of strongly southward IMF, with one in the compressed sheath region and one in the magnetic cloud (Kataoka et al., 2015). On 17 March 2015, the *Sym-H* index reached −234 nT at 22:47 UT (Figure 1d) which made this storm the strongest of solar cycle 24.

The ICME arrived Earth at 4:48 UT as annotated by the sudden increase of solar wind speed (from 400 to 500 km/s) and the dynamical pressure (from 5 to >10 nP). The ICME arrival time is indicated by the vertical cyan line in Figure 1. The IMF was northward when the ICME hit the magnetosphere. Around 6 UT IMF B_z turned southward, the *Sym-H* index started to decrease, and the storm main phase started.

In the present study, we focus on the second IMF southward turning (gray-shaded area in Figure 1), which started at around 12 UT. The IMF B_z was strongly negative (from −3 nT at 12:00 UT to −25 nT after 12:30 UT) with a brief northward turning around 13:40 UT. The strongly southward IMF B_z favors dayside magnetopause reconnection, where the auroral oval and the convection cells are expected to expand equatorward (e.g., Cowley & Lockwood, 1992). Figure 1c shows that the *AE* index peaked at 13:58 UT at 2,298 nT, which indicates very intense substorm activity.

Figures 1e–1h show the GPS data from Skibotn in northern Norway. The different colors represent different GPS satellites, identified with the Pseudo Random Noise (PRN) codes in the color bar on the right side. The TEC data show a clear diurnal variation, that is, the TEC maximizes in the local noon/postnoon sector (around 10 UT) as for quiet times (see Figure S1 in the supporting information). However, the storm time TEC values were much higher than the quiet time ones (up to ~35 TECU [total electron content unit, 1 TECU = 10^{16} el m^{-2}] vs. up to ~20 TECU). This may be related to the positive storm effect of the ionosphere by which the electron density is greatly enhanced (e.g., Liu et al., 2016). There was a small TEC variation when the ICME hit the magnetopause, which is clearly shown by the ROT data in Figure 1f. This is related to the shock aurora that forms due to the compression of the magnetosphere by the interplanetary shock (see, e.g., Jin, Zhou, et al., 2016). However, significant amplitude and phase scintillations were not observed during this time.

The more rapid TEC variations were also different from the quiet time ones, as can be seen in the ROT data in Figure 1f. At night, Skibotn is located under the auroral oval, where there is often considerable ROT activity

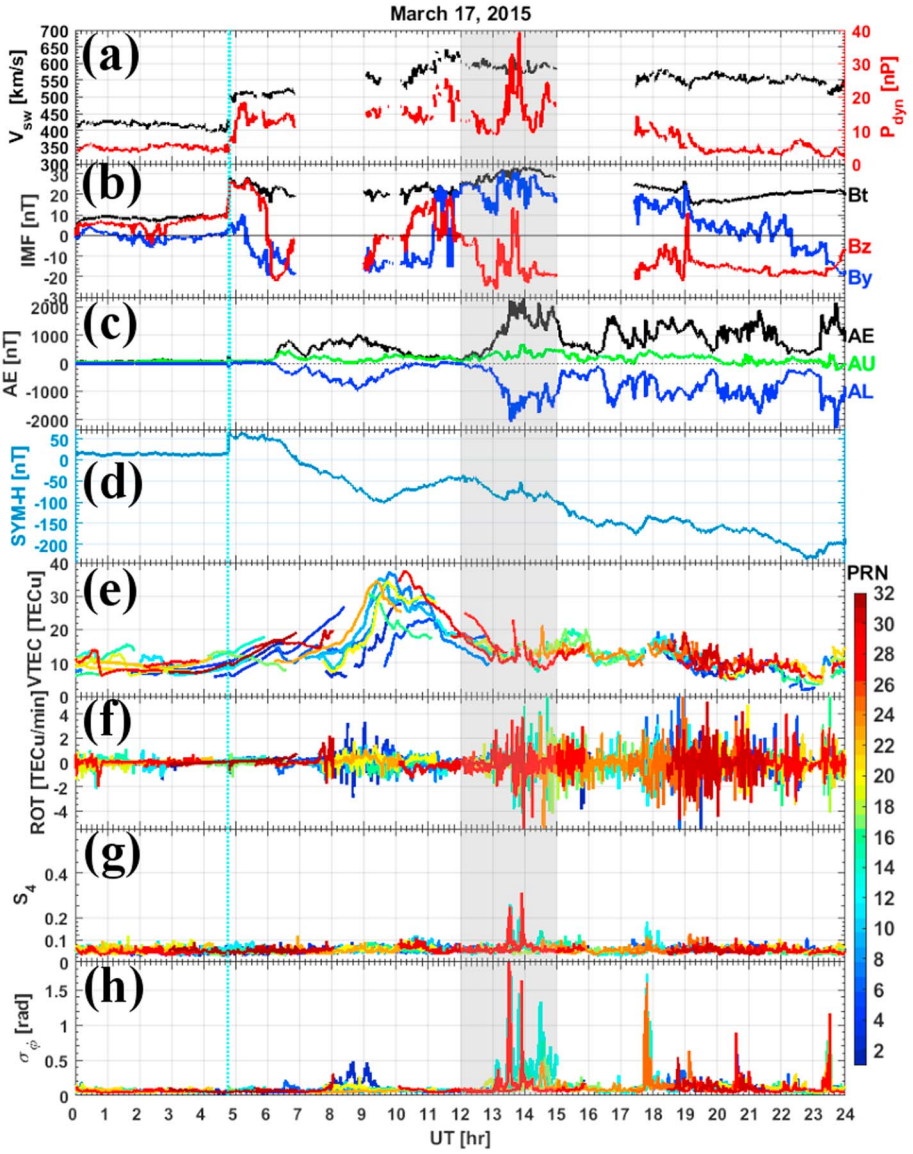

Figure 1. Overview of the event on 17 March 2015. (a) The solar wind speed (V_{sw}, black) and dynamical pressure (P_{dyn}, red). (b) The OMNI IMF data. (c) Magnetic *AE* indices. (d) The *Sym-H* index. (e–h) the GPS TEC, rate of change of TEC (ROT), and amplitude (S_4) and phase scintillation indices (σ_ϕ) from Skibotn in northern Norway. The vertical cyan line shows the storm sudden commencement at 4:48 UT. The gray shaded region highlights the interval of the second southward IMF turning, which is the focus in this paper. IMF = interplanetary magnetic field; GPS = Global Positioning System; TEC = total electron content; VTEC = Vertical total electron content.

(Jacobsen & Dähnn, 2014). On the dayside, Skibotn is equatorward of the auroral oval, where the ROT activity is usually very low. However, during the St. Patrick's Day storm, the ROT activity was very high also on the dayside (8–10 UT and 13–15 UT). Significant scintillations were also observed during the storm main phase. From 8 to 10 UT, the GPS phase scintillations (σ_ϕ) were moderate with low or no amplitude scintillations (S_4). This is often the case at high latitudes (Spogli et al., 2009; van der Meeren et al., 2014). From 13 to 15 UT, the GPS phase scintillations were very high and pulsed (often exceeding 1.5 rad), and the amplitude scintillations were also very significant (up to 0.3). We will therefore focus on this time period in the following and elaborate on the intense scintillation scenario of significant and coexisting amplitude and phase scintillations. The scintillation scenarios at other times during this storm are described by Jacobsen and Andalsvik (2016) and Prikryl et al. (2016).

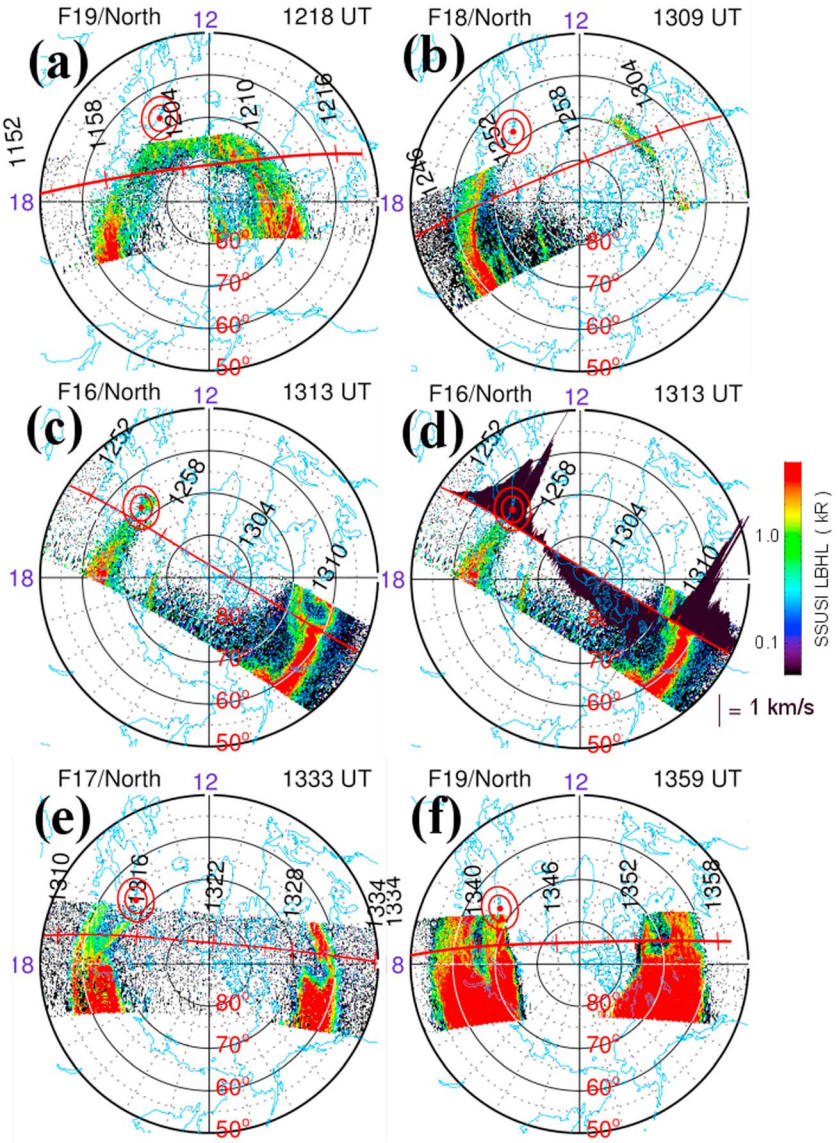

Figure 2. Auroral images from SSUSI and cross-track ion flow vectors from ion drift meter onboard the DMSP satellites. The data are plotted in MLAT-MLT coordinates with coastlines overlaid. The DMSP orbits are plotted as red lines in each panel, with time annotated at 6 min cadence along the satellite track. The red circles show the fields of view of Skibotn for elevation angles of 30° and 45° and projected to 350 km altitude, and the red dot shows the location of Skibotn. SSUSI = Special Sensor Ultraviolet Spectrographic Imager; DMSP = Defense Meteorological Satellite Program; MLAT = magnetic latitude; MLT = magnetic local time; LBHL = Lyman-Birge-Hopfield long filter band.

As it was shown in Figure 1b, the IMF B_z turned strongly southward from 12:30 UT onward. As a response to the southward IMF B_z, the auroral oval and the ionospheric convection cell expanded considerably (see, e.g., Hairston et al., 2016). Figure 2 displays the auroral images from the SSUSI instrument and cross-track ion flow vectors from the ion drift meter onboard the DMSP satellites. Figure 2a from DMSP F19 corresponds to the time just before the IMF became strongly southward. The auroral image shows a clear dayside auroral oval with the equatorward boundary at around 70° MLAT. The red circles in the afternoon sector (around 13–15 magnetic local time [MLT]) indicate the fields of view of Skibotn at elevation angles of 30° and 45°. The dayside aurora was mostly located poleward of Skibotn, and the aurora only covered the northern part of the field of view. We regard the auroral oval in Figure 2a as our baseline. DMSP F18 came ~51 min later, as shown in Figure 2b. The auroral oval expanded equatorward of 70° MLAT, but there was no direct overlap in terms of fields of view for SSUSI and Skibotn. However, if we interpolate the auroral oval from 17 MLT to the location of

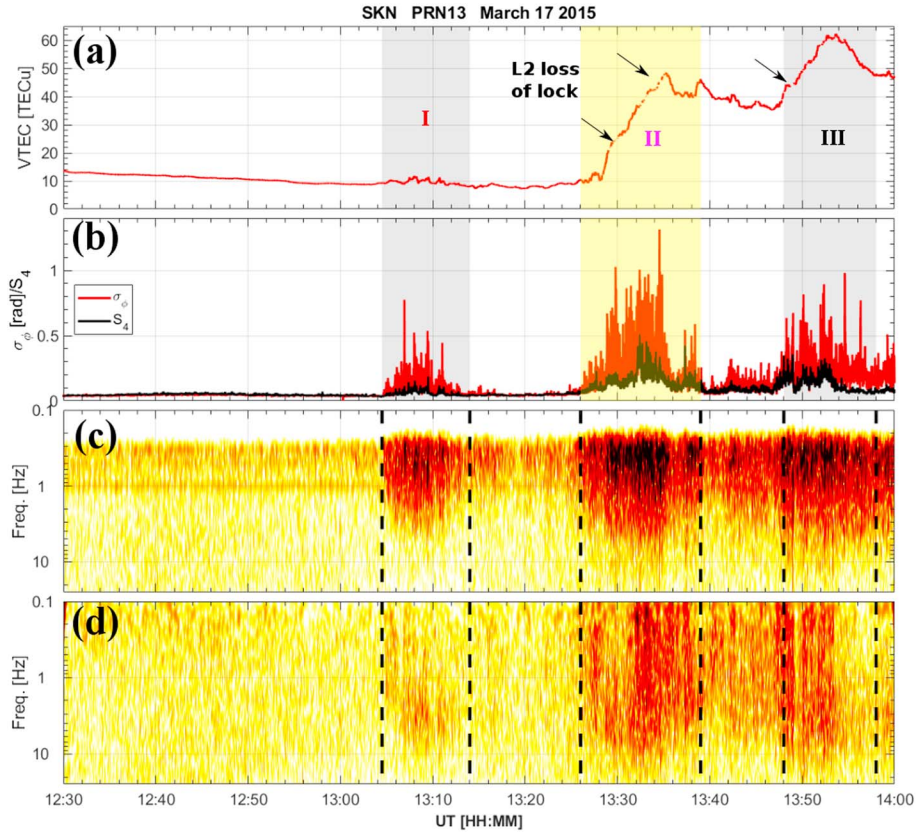

Figure 3. Data from GPS PRN13. (a) The 1-s resolution TEC data. (b) The 1-s resolution amplitude (S_4, black) and phase (σ_ϕ, red) scintillation indices. The phase scintillation indices are calculated by detrending the raw data using a high-pass Butterworth filter with a cutoff frequency of 0.3 Hz. (c) A spectrogram of the carrier phase data. (d) A spectrogram of the received signal amplitude. GPS = Global Positioning System; PRN = pseudo random noise; TEC = total electron content; VTEC = Vertical total electron content.

Skibotn, the aurora should be located over Skibotn (66° MLAT). DMSP F16 came 4 min later, and the SSUSI data now covered most of the Skibotn field of view, confirming that the auroral oval covered Skibotn at least from 12:55 UT.

The DMSP satellites also measure the cross-track ion flow. As an example, we show in Figure 2d the cross-track ion flow data from DMSP F16. The ion flow was characterized by antisunward flow in the central polar cap and sunward return flow in the dawn and dusk flanks. The ion flow was significantly enhanced compared to earlier times (see, e.g., Hairston et al., 2016). The ion velocity over Skibotn reached up to 3,000 m/s. The high flow velocity may cause strong ion-frictional heating and enhanced ion temperature (e.g., St.-Maurice & Hanson, 1982; Carlson, 2012; Bjoland et al., 2015). The enhanced ion temperature can cause rapid recombination of the ionosphere and depletion of the electron density (Rodger et al., 1992; Zou et al., 2017).

Figure 2e shows that the auroral oval continued its expansion, and the equatorward boundary reached 60° MLAT. The duskside oval was also likely split in two parts. Figure 2f shows that the duskside oval expanded further, and the double oval intensified and widened from 13:38 to 13:44 UT. At this time it was likely that the whole Skibotn field of view was covered with intense auroral activity.

Next, we present the scintillation data of a selected GPS satellite (PRN13). Figures 3a and 3b show the 1-s resolution TEC, amplitude (S_4) and phase (σ_ϕ) scintillation indices observed from Skibotn, while Figures 3c and 3d show the spectrograms of the detrended carrier phase and amplitude using a Morlet wavelet. The TEC decreased slowly from 12:30 to 13:00 UT, and there was no phase and amplitude scintillations. From 13 to 14 UT, three intervals were observed of enhanced TEC fluctuations, intensified phase and amplitude scintillations, and enhancements in the power spectral density (PSD) of phase and amplitude. The three intervals are shaded and labeled as I, II, and III in Figure 3. In interval I (13:02–13:12 UT) the TEC displays small

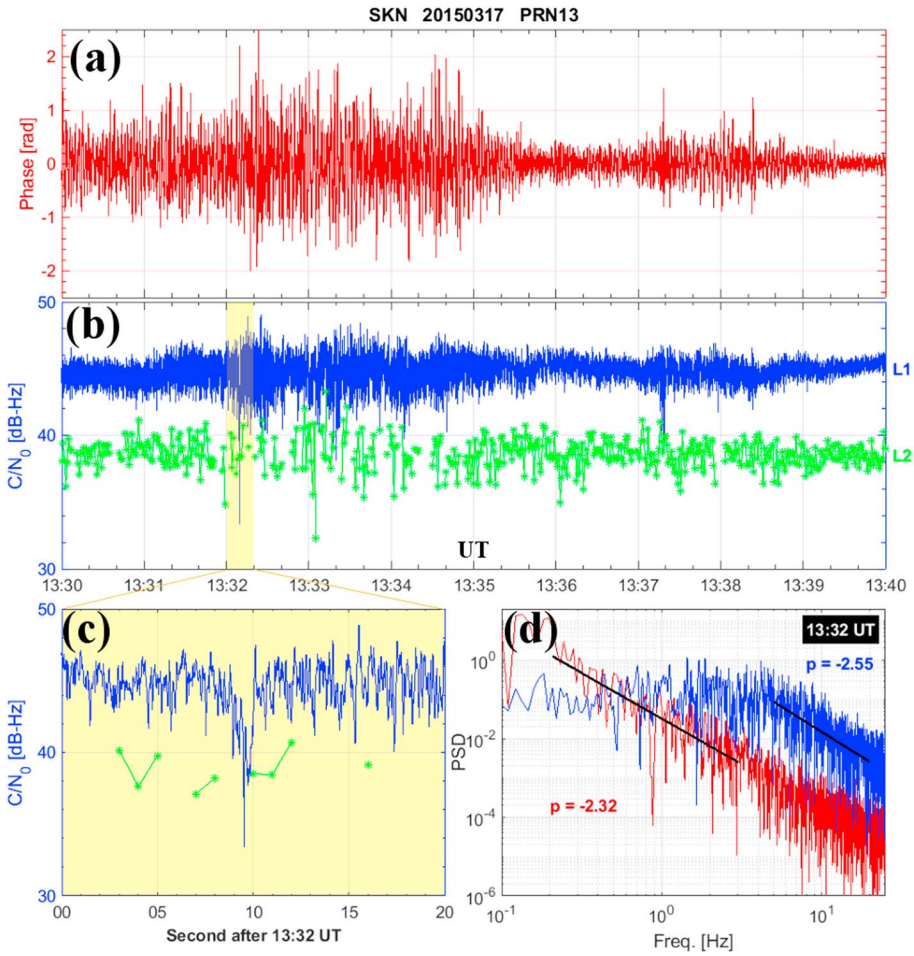

Figure 4. (a) The filtered GPS carrier phase data using a high-pass Butterworth filter with a cutoff frequency of 0.3 Hz. (b) the received signal power in terms of carrier-to-noise density (C/N_0) at L1 (blue) and L2 (green), respectively. The yellow shaded region highlights the period of significant amplitude scintillation in the L1 band, and the data are enlarged in panel (c) to demonstrate the signal power fade. (d) The power spectra and fitted spectral slopes of the phase (red) and amplitude (blue). See text for more details. GPS = Global Positioning System.

fluctuations and the scintillation indices show significant phase scintillation (σ_ϕ) and weak amplitude scintillation (S_4). The spectrograms of the carrier phase and amplitude also display obvious enhancements in the PSD from 10 to 0.3 Hz (cutoff frequency of the Butterworth filter). In interval II the TEC was significantly enhanced and several losses of lock were observed in the L2 band (see gaps annotated by arrows in Figure 3a). Due to the losses of lock at the L2 frequency, the TEC data may be wrongly leveled and the TEC values may be too high after 13:30 UT. The TEC values can be verified against the TEC map in Figure 6c, where the TEC values were indeed enhanced near PRN13; however, the TEC enhancements of ~22 TECU seems to be more realistic. Figure 3b shows very strong GPS phase scintillation (up to 1.4 rad) and significant amplitude scintillation (up to 0.5) in interval II. The spectrogram of phase shows enhanced PSD from 0.3 up to 20 Hz, and the spectrogram of the amplitude shows enhancement at all scales. Interval III was very similar to interval II, but it exhibits slightly weaker phase and amplitude scintillations.

We next focus on the strongest amplitude and phase scintillations in interval II. Figures 4a and 4b show the detrended carrier phase and raw received signal power in terms of carrier-to-noise density (C/N_0) in the L1 band during 13:30–13:40 UT. Both the detrended carrier phase (red) and received signal power (blue) show significant fluctuations, and the highest signal power fade occurred around 13:32.10 UT (shaded in yellow). Figure 4c presents an expanded plot for the interval 13:32.00–13:32.20 UT when significant power fade was observed due to the destructive diffraction. The received power decreased from 45 to 33 dB-Hz in less

than 1 s. However, this power level is still higher than the threshold required to maintain the tracking lock (Kintner et al., 2007).

For completeness, the received signal power in the L2 band is also shown in green in Figures 4b and 4c. The receiver only records the signal power in the L2 band at 1-s resolution. The signal power in the P code L2 band is generally lower than the signal in the C/A code L1 band (Kintner et al., 2007). In this situation, the received power in the L2 band was lower by ~6 dB-Hz than the L1 band signal. The C/N_0 in the L2 band shows larger fluctuations and clear losses of lock as discontinuities in the signal power. Figure 4c shows that losses of lock in the L2 band lasted for up to several seconds when significant signal fade occurred in the L1 band.

To illustrate the typical characteristics of the GPS scintillation spectra, Figure 4d shows the power spectra of the carrier phase (red) and amplitude (blue) during 13:32–13:33 UT. The spectra are obtained by using a fast Fourier transform. The PSD of the carrier phase is monotonously decreasing as the frequency increases. However, the PSD of the amplitude is more or less flat from 0.1 to 5 Hz, and it is decreasing for higher frequencies. This is the so-called Fresnel filtering effect on the amplitude scintillation, where the amplitude scintillation is caused by irregularity scales lower than the Fresnel radius (e.g., Basu et al., 1994; Kintner et al., 2007; Wernik et al., 2008). The Fresnel radius is defined as $r_f = \sqrt{2\lambda z}$, where λ is the signal wavelength (0.19 m for the GPS L1 band), and z is the slant distance from the receiver to the irregularity phase screen. The frequency above which the PSD begins to decrease is known as the Fresnel frequency (f_F), which in our case is f_F = 5 Hz. We can derive the relative drift speed (v) between the irregularity and line of sight of the GPS satellite perpendicular to the ray path by using the formula $v = f_F * r_f$. By assuming an irregularity layer at 350 km altitude, and using the elevation angle of PRN13 (63°), the relative drift speed is found to be around 1,370 m/s. This is similar to the ion flows observed by DMSP F16.

The spectra of the GPS carrier phase are often presented in the form of a power law (f^p), and we fit the spectral slope in the frequency range [0.2, 3] Hz by the black line in Figure 4d. The spectral slope p is -2.32. By the same token, we fit the PSD of the amplitude (blue) in the frequency range [5, 15] Hz. The spectral slopes of the carrier phase and amplitude are similar but not exactly the same. This is probably due to slightly different fitting intervals and background noise levels of the phase and amplitude measurements (see, e.g., Jayachandran et al., 2017).

Figure 5 shows another example of significant scintillations from GPS PRN28, which was located around 192 km east of PRN13 (see Figure 7). It also observed three intervals of enhanced TEC fluctuations, as well as significant amplitude and phase scintillations (13:03–13:13 UT, 13:28–13:33 UT, and 13:51–13:53 UT). These intervals are shaded and labeled as I′, II′, and III′ in Figure 5. For intervals II′ and III′, losses of lock occurred at the L2 frequency and the phase scintillations exceeded 1 rad, while the amplitude scintillations reached up to 0.5. The spectrograms of phase and amplitude data in Figures 5c and 5d show significant fluctuations at all scales during intervals II′ and III′.

In Figure 6 we present large-scale TEC maps to illustrate the plasma processes when strong phase and amplitude scintillations were observed during interval II. The phase scintillation data are also overlaid in each panel using different symbols, with red five-pointed stars presenting strong phase scintillations. In this figure, we make use of the phase scintillation data from Skibotn (SKN), as well as GPS and GLONASS phase scintillation data from Ny-Ålesund (NYA), Longyearbyen (LYB), Hopen (HOP), and Bjørnøya (BJN). The five stations are shown by crosses in each panel of Figure 6 and annotated in Figure 6b.

At 12:12 UT the TEC was moderate in northern Scandinavia (~17 TECU), and the auroral oval was located well poleward of Skibotn (cf. Figure 2a). Low scintillation levels were observed from NYA, LYB, HOP, and BJN; the phase scintillation equatorward of 70° MLAT was very quiet. As the auroral oval and convection cell expanded equatorward, Skibotn came inside the auroral oval and the strong ion flow region at 13:22 UT (cf. Figure 2d). The ionospheric density was depleted due to enhanced recombination as a consequence of strong convection. At this time the scintillations were still low near Skibotn. At 13:32 UT the TEC near Skibotn suddenly increased and strong phase scintillations were observed near the TEC enhancement. The TEC enhancement faded gradually and the scintillation faded as well, as shown in Figure 6d. The TEC enhancement was unlikely to be caused by the particle impact ionization since it had a completely different shape than the aurora in Figure 2. However, the particle precipitation may have contributed to some of the TEC enhancement. An animated TEC map in the same format as Figure 6 for interval II is shown in Movie S1 in the supporting

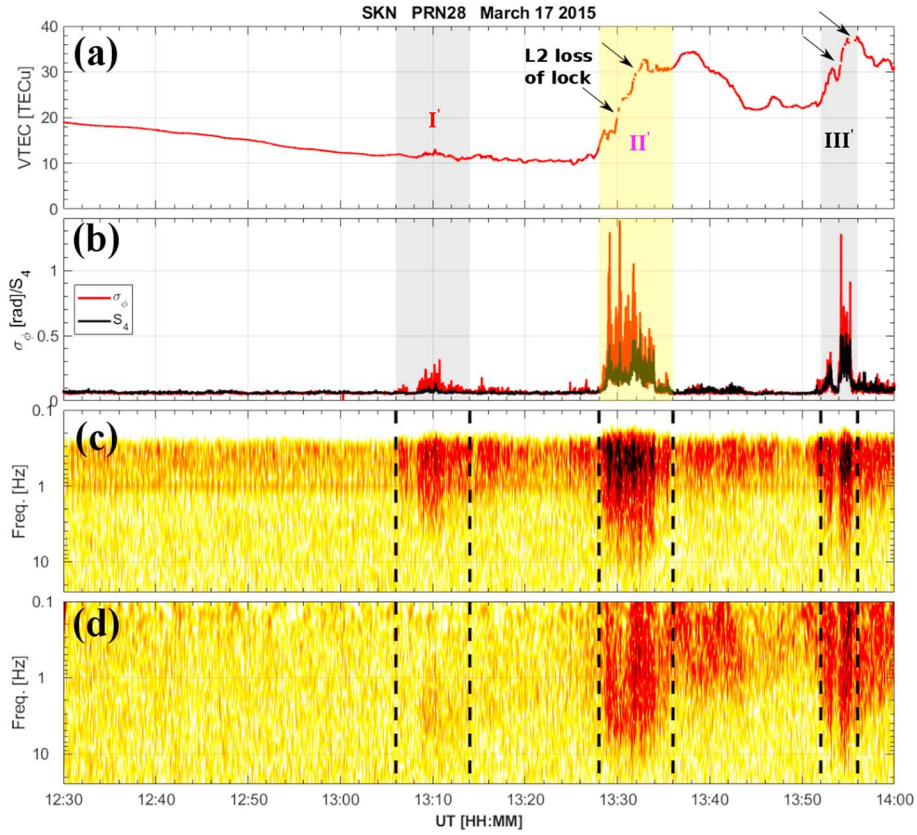

Figure 5. Same format as Figure 3, but for GPS PRN28. GPS = Global Positioning System; PRN = pseudo random noise; VTEC = Vertical total electron content.

information. Movie S1 shows that the TEC enhancement was mainly caused by poleward transport of dense plasma from lower latitudes.

4. Discussion

The previous section showed that the auroral oval expanded significantly equatorward in response to the strongly southward IMF B_z after 12:30 UT during the 17 March 2015 St. Patrick's Day storm. The auroral oval was over Skibotn at least from 12:56 UT (cf. Figure 2). From 13 to 14 UT, we observed three main intervals (labeled I, II, and III in Figures 3 and 5) of enhanced amplitude and phase scintillations, with interval II as the strongest one.

In interval II the TEC map shows a blob of high TEC values that propagated poleward and into the Skibotn field of view. At the same time, the TEC around Skibotn quickly intensified. Significant scintillations (S_4 up to 0.5, σ_ϕ up to 1.4 rad) were observed near the edges of the TEC blob. The auroral images from DMSP satellites indicate that the TEC blob occurred in the auroral oval. However, the enhanced TEC was unlikely due to local auroral particle precipitation since the shape of the enhanced ionization was very different from the auroral morphology. In addition the TEC map in the supporting information shows a clear poleward propagation of an area of enhanced TEC, which suggests that the TEC enhancement originated at lower latitudes.

Note that the TEC is the integrated electron density along the line of sight between the GPS satellites and the ground receiver. It is not possible to resolve the vertical electron density profile of the TEC blob based solely on the TEC map. Fortunately, the EISCAT UHF radar operated during our time of interest. It was pointing in a fixed direction along the local magnetic field in the *F* region (azimuth 185°, elevation 77°). The observation geometry is shown in Figure 7 where the locations of the radar site at Tromsø (TRO) and the radar beam at 350 km altitude (referred to as UHF) are annotated. The distances between each point are also annotated. Both UHF and PRN13 were near the edge of the TEC blob, and they were only 94 km ($<$ 1° in latitude)

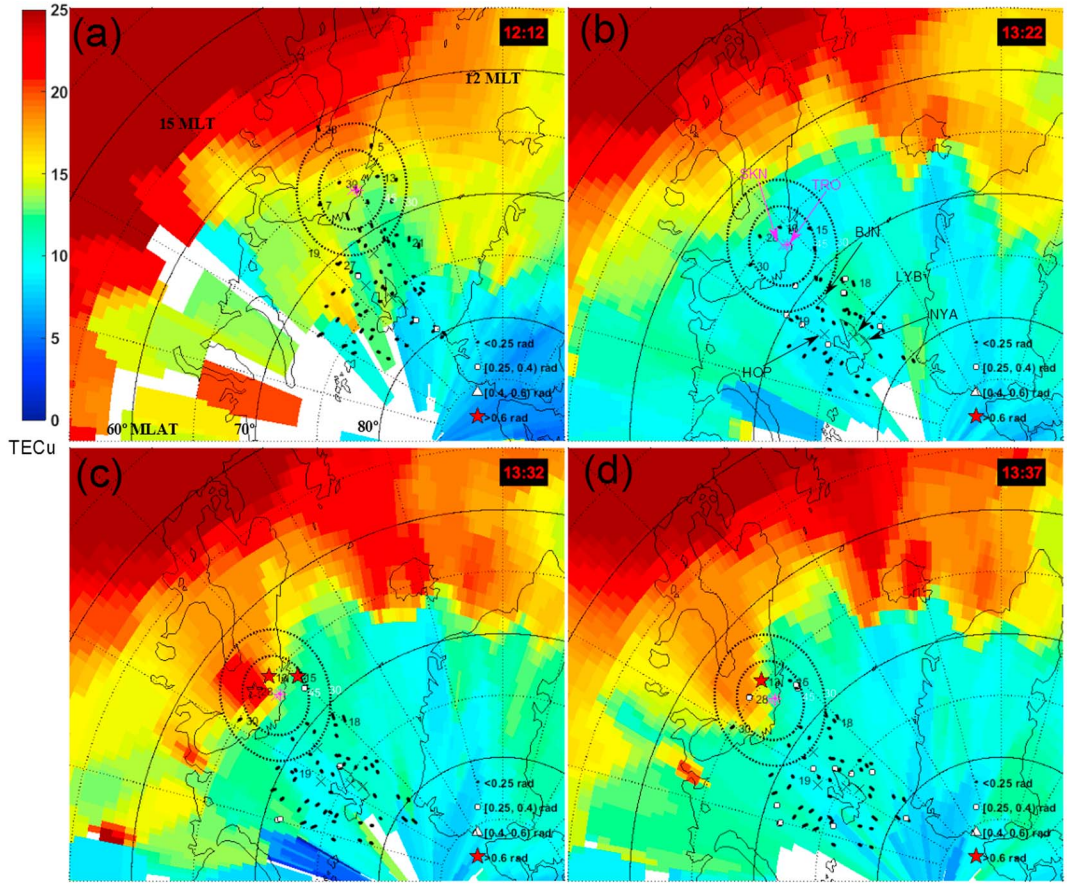

Figure 6. TEC maps at four selected times. The UT time is shown in the top right comer of each panel, and the map is using MLAT-MLT coordinates. The TEC data are obtained from the Madrigal database. Phase scintillation data are overlaid with different symbols according to the phase scintillation strength as indicated in the bottom right corner of each panel. The scintillation data are from five stations as annotated in panel (b): SKN = Skibotn; BJN = Bjørnøya; HOP = Hopen; LYB = Longyearbyen; NYA = Ny-Ålesund. The SKN fields of view at elevation angles of 30° and 45° are shown in each panel as dotted circles. TEC = total electron content; MLAT = magnetic latitude; MLT = magnetic local time; TRO = Tromsø.

away from each other. We can therefore use the UHF observation to infer the electron density profile in the vicinity of the PRN13 line of sight.

Figure 8 shows the ionospheric parameters (electron density Ne, electron temperature Te, and ion temperature Ti) from the UHF radar as a function of altitude from 12:00 UT to 13:50 UT, when it stopped operation. From 12:00 UT to 12:50 UT the UHF radar observed a typical smooth and cold subauroral ionosphere (low Ti and Te). The subauroral ionospheric plasma faded out gradually due to the strong ion velocity (cf. Figure 2d). The enhanced Ti indicates strong Joule heating, and the electron density depleted as a result of rapid recombination (e.g., Rodger et al., 1992). From 12:50 UT onward, the auroral oval covered the vicinity of the radar beam (cf. Figure 2), and the observed plasma was structured in both the *E* and *F* regions, with enhanced Te indicating ongoing electron precipitation, and enhanced Ti indicating strong Joule heating. Schunk et al. (1975) simulated the effect of strong electric fields (ion velocity) on the daytime high-latitude ionosphere. During strong electric field, the ionospheric electron density decreases at all altitudes; however, the depletion of electron density is most intense in the F_2 region. The height of the peak electron density decreases toward 200 km when the electric field is larger than 50 mV/m (equivalent to an ion flow speed of 1,000 m/s). The changed electron density profile in Figure 8a perfectly match that simulation, that is, the topside electron density decreased gradually and left a thin plasma layer at around 200 km altitude (see Figure 8 of Schunk et al., 1975).

Following the labelling in Figure 3, we highlight the same scintillation intervals I, II, and III in Figure 8. However, the UHF data only covers a very small part (2 min) of interval III. For this reason we focus on the

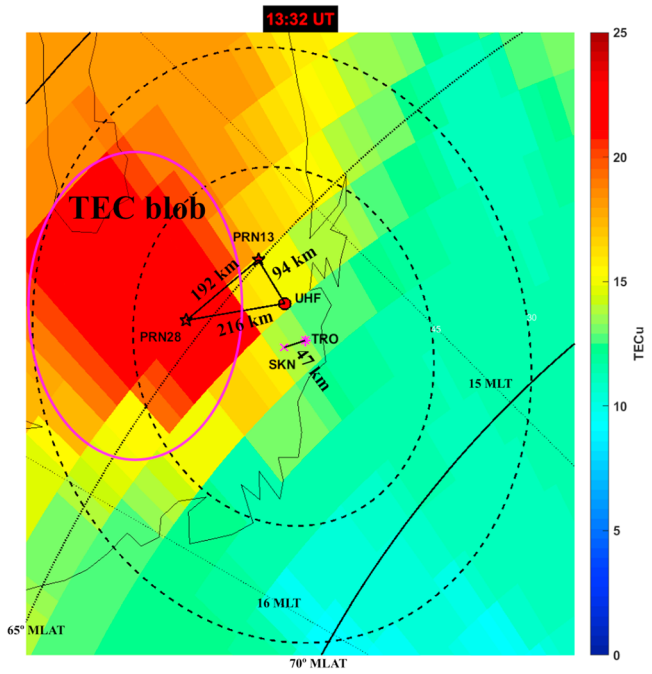

Figure 7. The observation geometry of the GPS satellites and the EISCAT UHF radar. The five-pointed stars show the ionospheric pierce points of PRN13 and PRN28 at 13:32 UT, assuming an ionospheric height of 350 km. The EISCAT radar site at Tromsø (TRO) and the GPS receiver at Skibotn (SKN) are shown in magenta asterisk and cross, respectively. The location of the UHF beam (azimuth = 185°, elevation = 77°) at 350 km altitude is shown by a red dot. The distances between each point are annotated. GPS = Global Positioning System; EISCAT = European Incoherent SCATter; UHF = ultrahigh frequency; TEC = total electron content; MLT = magnetic local time; PRN = pseudo random noise.

first two intervals. From the UHF data, both intervals I and II were associated with enhanced Ti which indicates strong ion velocity and/or velocity shear. The enhanced Te indicates that active electron precipitation was present. The enhancement in the F_2 region (300–500 km) was especially clear during interval II. From the TEC map (Figure 7), we know that the enhancement at the F_2 layer was due to the TEC blob.

In Figure 9 we plot several electron density profiles in order to better differentiate the altitude dependence. The gray line is an average for 13:15–13:25 UT, which represents the background condition between intervals I and II. The density profile shows a single peak around 220 km altitude. The colored lines show that the density at 200 km was slightly enhanced during interval II, with a small density enhancement around ~120 km indicating energetic electron precipitation. However, the most obvious change from the background density profile is the topside ionosphere, where the density at 400 km was greatly enhanced (from 0.8×10^{11} to 1.6×10^{11} m^{-3}). This satisfies the definition of plasma blobs or patches, that is, the electron density must be enhanced by at least 2 times the background (Crowley et al., 2000).

This observation is consistent with Jin et al. (2017) who observed significantly enhanced phase scintillations when polar cap patches formed near the cusp inflow region. The difference is that Jin et al. (2017) used the EISCAT Svalbard Radar at 75° MLAT, while the current study uses the EISCAT UHF radar at 66° MLAT. Therefore, Jin et al. (2017) investigated the plasma status near the cusp latitude around magnetic noon, while the current paper studies the scintillation effect in the afternoon sector (15–16 MLT) during a strong geomagnetic storm. This scenario is also similar to the one reported by Jin et al. (2014) who observed enhanced phase scintillations when high-density polar cap patches entered into the auroral oval during nighttime. In the current study, the strong scintillations were observed near the edges of the enhanced TEC blob and the UHF radar observed significant enhancement in the F_2 region plasma. We conclude that the F_2 layer plasma plays an important role in producing scintillations. An extensive discussion of the possible instability modes is out of the scope of the current study. However, the plasma processes should be similar to Jin et al. (2014, 2017) and Jin, Moen, et al. (2016). Since the F_2 region plasma enhancement was the main feature of the strong scintillations, the instability modes should relate to the F_2 region (Basu et al., 1998) in addition to structured particle precipitation.

It should be noted that even though the UHF radar beam and PRN13 were very close (94 km), they were still not measuring plasma along the exact same line of sight. Recently, Forte et al. (2016) made an experiment by using the EISCAT UHF radar and a colocated GPS receiver, in which they pointed the EISCAT radar toward a given GPS satellite, and therefore the GPS receiver and EISCAT measured the electron density along the same line of sight. In this way, the comparison between the EISCAT and the GPS receiver was more accurate than the configuration of UHF and PRN13 in the current study. However, they did not observe any GPS amplitude scintillation in their experiment. It is worthwhile to test this experiment setup in the future during intervals of strong GPS amplitude and phase scintillations.

In the current event, we observed both significant phase and amplitude scintillations. The phase scintillations are caused by electron density irregularities of scale size ranging from hundreds of meters to several kilometers, while the amplitude scintillations are caused by irregularities of scale size from tens of meters to hundreds of meters (Fresnel radius) due to the Fresnel filtering effect (Kintner et al., 2007). The observation of both amplitude and phase scintillations indicates that significant plasma irregularities were present at all scales. Indeed, the spectrograms of phase and amplitude data shows enhanced PSD over a full range of scales up to the Nyquist frequency of the data resolution (25 Hz). Both phase and amplitude scintillations could affect the tracking performance of the GPS receiver.

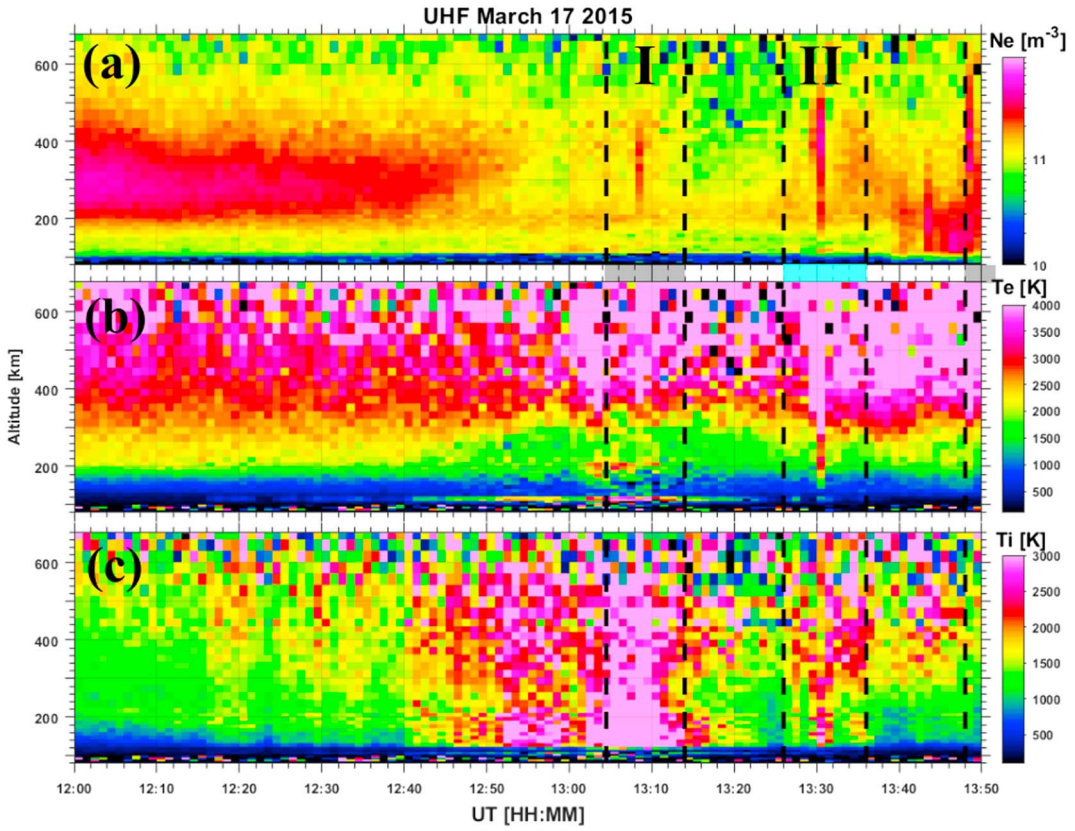

Figure 8. The EISCAT UHF data: (a) electron density (Ne), (b) electron temperature (Te), and (c) ion temperature (Ti). The radar was pointing in a fixed direction (azimuth 185°, elevation 77°), which corresponds to the magnetic field-aligned direction in the *F* region. The UHF data have been postprocessed at 1-min time resolution. The vertical dashed lines mark the same time intervals as in Figure 3. EISCAT = European Incoherent SCATter; UHF = ultrahigh frequency.

By looking at the received signal power at the L1 band, we find that the signal power decreased from 45 to 33 dB-Hz in less than 1 s due to the destructive interference after the radio wave passed through the plasma irregularities. However, the GPS receiver was still able to maintain tracking of the GPS L1 signal (1.57542 GHz). Losses of lock in the L2 band (1.2276 GHz) occurred frequently for several satellites (PRN13, PRN28, and others not shown), and it was especially obvious in interval II for PRN13. The differences between the two frequencies can be explained as follows: first, the ionospheric scintillation is dependent on the signal frequency and the lower frequency signals are more severely affected by the same scintillating structures (Kintner et al., 2007; Yeh & Liu, 1982); second, the signal power in the GPS L2 band is lower than in the L1 band, which makes the L2 band more vulnerable to ionospheric scintillation than the L1 band (Kintner et al., 2007).

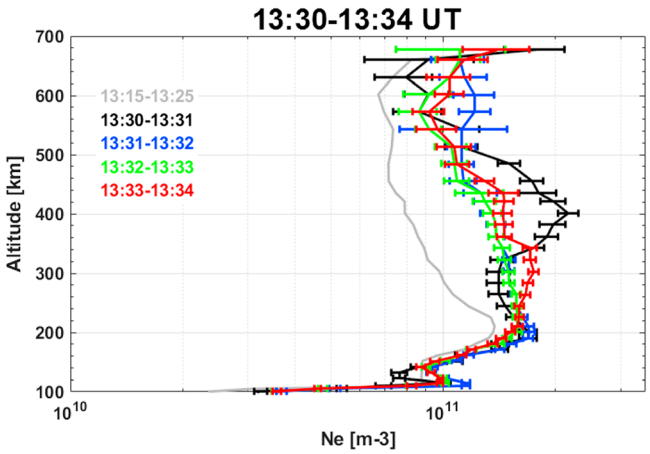

Figure 9. Electron density profiles from the EISCAT UHF radar in interval II. The measurement uncertainties are represented by error bars. The time periods are annotated to the left. EISCAT = European Incoherent SCATter; UHF = ultrahigh frequency.

Unfortunately, we do not have high-resolution measurements of the received signal power in the L2 band. Nonetheless, the 1 Hz C/N_0 in the L2 band indeed decreased. Both deep signal power fades and rapid phase fluctuations can lead to loss of lock of GPS signal. However, due to the low resolution (1 s), it is difficult to conclude whether the losses of lock were due to lower signal power or due to rapid phase fluctuation. The relative closeness in Fresnel scales of the L1 and L2 signals means that the amplitude scintillations for received L1 and L2 signals should be similar as well. By subtracting the nonscintillating signal power at L2 band (39 dB-Hz) by the fade of 12 dB-Hz, we get 27 dB-Hz, which is close to the threshold to maintain the signal tracking (Kintner et al.,

2007). The losses of lock also occurred when the power fades were much less than 12 dB-Hz, which implies that the rapid phase fluctuation should also contribute to losses of lock of GPS signals. It should be noted that even though our GPS scintillation receiver could track the GPS signal at L1 band, a normal GPS receiver may not be able to track the signal since our scintillation receiver is specially designed to track signals during strong scintillations (e.g., Datta-Barua et al., 2014; Van Dierendonck et al., 1993). Further studies are necessary to characterize the tracking performance of the GNSS receiver under strong ionospheric scintillations, which can provide important guidelines for the development of future GNSS receivers.

5. Summary and Concluding Remarks

We have presented a case study of the GPS amplitude and phase scintillations at high latitudes during the main phase of a major geomagnetic storm (*Sym-H* was −234 nT). We focused on a period of strongly southward IMF (B_z was −25 nT) using comprehensive measurements from space and ground. The auroral oval expanded significantly equatorward, and the aurora covered northern Norway at ~15 MLT, which normally would be in the subauroral region for nonstorm conditions at this local time. Auroral images from the SSUSI instrument onboard DMSP satellites allowed us to locate the observations with respect to the auroral oval. The global TEC data and a regional network of scintillation receivers revealed an area of strong GPS scintillations, which was coincident with the EISCAT radar field of view, and allowed a very detailed analysis of the prevailing ionospheric conditions and the detailed scintillation effects on GPS signals.

The GPS data from Skibotn in northern Norway showed three intervals of enhanced TEC fluctuations and significant scintillations during 13–14 UT. Unlike earlier studies at high latitudes that mainly have focused on less active geomagnetic conditions, this major storm had significant amplitude scintillation of GPS signals in addition to phase scintillation. In the GPS L2 band the receiver lost lock many times due to power fading. However, in the GPS L1 band the receiver maintained successful tracking of signals despite significant amplitude scintillation (the 1-s resolution S_4 reached above 0.5) and power fade (12 dB-Hz). The TEC map allowed us to identify that the most significant scintillations occurred near the edge of a TEC blob, which was a region of enhanced TEC that originated from lower latitudes and propagated poleward. The EISCAT UHF data confirm that the enhanced electron density in the F_2 region meets the definition of plasma blob or patch; hence, we associate the severe amplitude scintillation to that plasma blob/patch.

In literature, significant GPS amplitude scintillations have been rarely observed at high latitudes (e.g., Forte & Radicella, 2002; Mitchell et al., 2005; van der Meeren et al., 2014). However, these studies have generally been carried out under much weaker geomagnetic activity. Our event was a major storm (the largest of the last solar maximum) where significant amplitude scintillations were coincident with strong phase scintillations (exceeding 1.5 rad). It indicates plasma irregularities extending over a wide range of spatial scales from kilometer to hectometer (close to the Fresnel scale) which can effectively produce both GPS phase and amplitude scintillations. The spectrograms of the phase and amplitude data display enhanced power from ~0.3 to ~20 Hz (cf. Figures 3c and 3d), which correspond to spatial scales of 4.6 km to 68.5 m (assuming a relative drift speed of 1,370 m/s; see section 3 for more details). Plasma irregularities were observed across all these scales.

We also would like to point out that the strongest GPS scintillations were found near the edge of a TEC blob. This highlights the importance of plasma blobs in disturbing satellite-based navigation systems. It is also in agreement with the recent findings that the auroral blobs cause the strongest GPS phase scintillations (Jin et al., 2014, 2017; Jin, Moen, et al., 2016). The significant equatorward expansion of the auroral oval made it easier to transport high-density solar extreme ultraviolet ionized plasma into the auroral oval. Auroral dynamics can effectively structure the entering high-density plasma. Further studies are needed to better understand plasma structuring of the F_2 region ionosphere inside the auroral oval, in particular during severe geomagnetic storms, when the auroral oval expands toward higher-density plasma at lower latitudes, which results in stronger irregularities, more amplitude scintillation, power fades, and loss of signal lock. This may require in situ electron density and electric field measurements (e.g., Moen et al., 2012).

Acknowledgments
The authors thank the Tromsø Geophysical Institute for assisting us with the GPS receiver in Skibotn, Bjørn Lybekk and Espen Trondsen for the instrument operation, and Charles Carrano for providing the GPS software. The research has received financial support from the Research Council of Norway under grant 230935. This research is a part of the 4DSpace Strategic Research Initiative at the University of Oslo. Yaqi Jin is partly supported by the Swarm Data, Innovation, and Science Cluster (DISC) project found by ESA. The IMF and solar wind data are provided by the NASA OMNIWeb service (http://omniweb.gsfc.nasa.gov). The GPS TEC data for the GPS TEC map can be obtained through the Madrigal database at Haystack Observatory (http://madrigal.haystack.mit.edu/madrigal/). The NovAtel GPStation 6 receivers at NYA, KHO, BJN, and HOP are supported by the Research Council of Norway under contracts 212014 and 223252, and the data may be obtained from Kjellmar Oksavik (e-mail: kjellmar.oksavik@uib.no). EISCAT is an international association supported by research organizations in China (CRIRP), Finland (SA), Japan (NIPR and STEL), Norway (NFR), Sweden (VR), and the United Kingdom (NERC). Data from EISCAT can be obtained from the Madrigal database http://www.eiscat.se/madrigal. The DMSP SSUSI data were obtained from The Johns Hopkins University Applied Research Laboratory (https://ssusi.jhuapl.edu/). The DMSP ion drift data were obtained from the NOAA (ftp://ftp.ngdc.noaa.gov/STP/satellite_data/). The authors also wish to thank the International Space Science Institute in Beijing (ISSI-BJ) for supporting the international team on "Multiple-instrument observations and simulations of the dynamical processes associated with polar cap patches/aurora and their associated scintillations," during which the discussions leading/contributing to this publication were initiated/held.

References

Alfonsi, L., Spogli, L., De Franceschi, G., Romano, V., Aquino, M., Dodson, A., & Mitchell, C. N. (2011). Bipolar climatology of GPS ionospheric scintillation at solar minimum. *Radio Science*, *46*, RS0D05. https://doi.org/10.1029/2010RS004571

Basu, S., Basu, S., Chaturvedi, P. K., & Bryant, C. M. Jr. (1994). Irregularity structures in the cusp/cleft and polar cap regions. *Radio Science*, *29*(1), 195–207. https://doi.org/10.1029/93RS01515

Basu, S., Weber, E. J., Bullett, T. W., Keskinen, M. J., MacKenzie, E., Doherty, P., et al. (1998). Characteristics of plasma structuring in the cusp/cleft region at Svalbard. *Radio Science*, *33*(6), 1885–1899. https://doi.org/10.1029/98RS01597

Bjoland, L. M., Chen, X., Jin, Y., Reimer, A. S., Skjæveland, Å., Wessel, M. R., et al. (2015). Interplanetary magnetic field and solar cycle dependence of Northern Hemisphere *F* region joule heating. *Journal of Geophysical Research: Space Physics*, *120*, 1478–1487. https://doi.org/10.1002/2014JA020586

Carlson, H. C. (2012). Sharpening our thinking about polar cap ionospheric patch morphology, research, and mitigation techniques. *Radio Science*, *47*, RS0L21. https://doi.org/10.1029/2011RS004946

Carrano, C. S., Anghel, A., Quinn, R. A., & Groves, K. M. (2009). Kalman filter estimation of plasmaspheric total electron content using GPS. *Radio Science*, *44*, RS0A10. https://doi.org/10.1029/2008RS004070

Cowley, S. W. H., & Lockwood, M. (1992). Excitation and decay of solar wind-driven flows in the magnetosphere-ionosphere system. *Annales de Geophysique*, *10*(1–2), 103–115.

Crowley, G., Ridley, A. J., Deinst, D., Wing, S., Knipp, D. J., Emery, B. A., et al. (2000). Transformation of high-latitude ionospheric *F* region patches into blobs during the March 21, 1990, storm. *Journal of Geophysical Research*, *105*(A3), 5215–5230. https://doi.org/10.1029/1999JA900357

Datta-Barua, S., Walter, T., Bust, G. S., & Wanner, W. (2014). Effects of solar cycle 24 activity on WAAS navigation. *Space Weather*, *12*, 46–63. https://doi.org/10.1002/2013SW000982

De Franceschi, G., Alfonsi, L., Rornano, V., Aquino, M., Dodson, A., Mitchell, C. N., et al. (2008). Dynamics of high-latitude patches and associated small-scale irregularities during the October and November 2003 storms. *Journal of Atmospheric and Solar - Terrestrial Physics*, *70*(6), 879–888. https://doi.org/10.1016/j.jastp.2007.05.018

Forte, B., Coleman, C., Skone, S., Häggström, I., Mitchell, C., Da Dalt, F., et al. (2016). Identification of scintillation signatures on GPS signals originating from plasma structures detected with EISCAT incoherent scatter radar along the same line of sight. *Journal of Geophysical Research: Space Physics*, *122*, 916–931. https://doi.org/10.1002/2016JA023271

Forte, B., & Radicella, S. M. (2002). Problems in data treatment for ionospheric scintillation measurements. *Radio Science*, *37*(6), 1096. https://doi.org/10.1029/2001RS002508

Greenspan, M. E., Anderson, P. B., & Pelagatti, J. M. (1986). Characteristics of the thermal plasma monitor (SSIES) for the Defense Meteorological Satellite Program (DMSP) spacecraft S8 through S10, tech. Rep. AFGL-TR-86-0227, air force Geophys. Lab., Hanscom air Force Base, Mass.

Hairston, M., Coley, W. R., & Stoneback, R. (2016). Responses in the polar and equatorial ionosphere to the March 2015 St. Patrick Day storm. *Journal of Geophysical Research: Space Physics*, *121*, 11,213–11,234. https://doi.org/10.1002/2016JA023165

Huuskonen, A., & Lehtinen, M. (1996). General incoherent scatter analysis and GUISDAP error estimates valid for high signal strengths. *Journal of Atmospheric and Terrestrial Physics*, *58*(1–4), 435–452. https://doi.org/10.1016/0021-9169(95)00047-X

Jacobsen, K. S., & Andalsvik, Y. L. (2016). Overview of the 2015 St. Patrick's Day storm and its consequences for RTK and PPP positioning in Norway. *Journal of Space Weather and Space Climate*, *6*, A9. https://doi.org/10.1051/swsc/2016004

Jacobsen, K. S., & Dähnn, M. (2014). Statistics of ionospheric disturbances and their correlation with GNSS positioning errors at high latitudes. *Journal of Space Weather and Space Climate*, *4*, A27. https://doi.org/10.1051/swsc/2014024

Jayachandran, P. T., Hamza, A. M., Hosokawa, K., Mezaoui, H., & Shiokawa, K. (2017). GPS amplitude and phase scintillation associated with polar cap auroral forms. *Journal of Atmospheric and Terrestrial Physics*, *164*, 185–191. https://doi.org/10.1016/j.jastp.2017.08.030

Jin, Y., Moen, J., & Miloch, W. J. (2014). GPS scintillation effects associated with polar cap patches and substorm auroral activity: Direct comparison. *Journal of Space Weather and Space Climate*, *4*, A23. https://doi.org/10.1051/SWSC/2014019

Jin, Y., Moen, J., & Miloch, W. J. (2015). On the colocation of the cusp aurora and the GPS phase scintillation: A statistical study. *Journal of Geophysical Research: Space Physics*, *120*, 9176–9191. https://doi.org/10.1002/2015JA021449

Jin, Y., Moen, J. I., Miloch, W. J., Clausen, L. B. N., & Oksavik, K. (2016). Statistical study of the GNSS phase scintillation associated with two types of auroral blobs. *Journal of Geophysical Research: Space Physics*, *121*, 4679–4697. https://doi.org/10.1002/2016JA022613

Jin, Y., Moen, J. I., Oksavik, K., Spicher, A., Clausen, L. B. N., & Miloch, W. J. (2017). GPS scintillations associated with cusp dynamics and polar cap patches. *Journal of Space Weather and Space Climate*, *7*, A23. https://doi.org/10.1051/swsc/2017022

Jin, Y., Zhou, X., Moen, J. I., & Hairston, M. (2016). The auroral ionosphere TEC response to an interplanetary shock. *Geophysical Research Letters*, *43*, 1810–1818. https://doi.org/10.1002/2016GL067766

Kamide, Y., & Kusano, K. (2015). No major solar flares but the largest geomagnetic storm in the present solar cycle. *Space Weather*, *13*, 365–367. https://doi.org/10.1002/2015SW001213

Kataoka, R., Shiota, D., Kilpua, E., & Keika, K. (2015). Pileup accident hypothesis of magnetic storm on 17 March 2015. *Geophysical Research Letters*, *42*, 5155–5161. https://doi.org/10.1002/2015GL064816

King, J. H., & Papitashvili, N. E. (2005). Solar wind spatial scales in and comparisons of hourly Wind and ACE plasma and magnetic field data. *Journal of Geophysical Research*, *110*, A02104. https://doi.org/10.1029/2004JA010649

Kintner, P. M., Ledvina, B. M., & de Paula, E. R. (2007). GPS and ionospheric scintillations. *Space Weather*, *5*, S09003. https://doi.org/10.1029/2006SW000260

Li, G. Z., Ning, B. Q., Ren, Z. P., & Hu, L. H. (2010). Statistics of GPS ionospheric scintillation and irregularities over polar regions at solar minimum. *GPS Solutions*, *14*(4), 331–341. https://doi.org/10.1007/s10291-009-0156-x

Liu, J., Wang, W., Burns, A., Solomon, S. C., Zhang, S., Zhang, Y., & Huang, C. (2016). Relative importance of horizontal and vertical transports to the formation of ionospheric storm-enhanced density and polar tongue of ionization. *Journal of Geophysical Research: Space Physics*, *121*, 8121–8133. https://doi.org/10.1002/2016JA022882

Mitchell, C. N., Alfonsi, L., De Franceschi, G., Lester, M., Romano, V., & Wernik, A. W. (2005). GPS TEC and scintillation measurements from the polar ionosphere during the October 2003 storm. *Geophysical Research Letters*, *32*, L12S0. https://doi.org/10.1029/2004GL021644

Moen, J., Oksavik, K., Abe, T., Lester, M., Saito, Y., Bekkeng, T. A., & Jacobsen, K. S. (2012). First in-situ measurements of HF radar echoing targets. *Geophysical Research Letters*, *39*, L07104. https://doi.org/10.1029/2012GL051407

Moen, J., Oksavik, K., Alfonsi, L., Daabakk, Y., Romano, V., & Spogli, L. (2013). Space weather challenges of the polar cap ionosphere. *Journal of Space Weather and Space Climate*, *3*, A02. https://doi.org/10.1051/swsc/2013025

Oksavik, K., van der Meeren, C., Lorentzen, D. A., Baddeley, L. J., & Moen, J. (2015). Scintillation and loss of signal lock from poleward moving auroral forms in the cusp ionosphere. *Journal of Geophysical Research: Space Physics*, *120*, 9161–9175. https://doi.org/10.1002/2015JA021528

Paxton, L. J., Morrison, D., Zhang, Y. L., Kil, H., Wolven, B., Ogorzalek, B. S., et al. (2002). Validation of remote sensing products produced by the Special Sensor Ultraviolet Scanning Imager (SSUSI)—A far-UV imaging spectrograph on DMSP F16. *P Soc Photo-Opt Ins*, *4485*, 338–348.

Prikryl, P., Ghoddousi-Fard, R., Kunduri, B. S. R., Thomas, E. G., Coster, A. J., Jayachandran, P. T., et al. (2013). GPS phase scintillation and proxy index at high latitudes during a moderate geomagnetic storm. *Annales de Geophysique*, *31*(5), 805–816. https://doi.org/10.5194/angeo-31-805-2013

Prikryl, P., Ghoddousi-Fard, R., Weygand, J. M., Viljanen, A., Connors, M., Danskin, D. W., et al. (2016). GPS phase scintillation at high latitudes during the geomagnetic storm of 17–18 March 2015. *Journal of Geophysical Research: Space Physics*, *121*, 10,448–10,465. https://doi.org/10.1002/2016JA023171

Prikryl, P., Jayachandran, P. T., Mushini, S. C., & Chadwick, R. (2011). Climatology of GPS phase scintillation and HF radar backscatter for the high-latitude ionosphere under solar minimum conditions. *Annales de Geophysique*, *29*(2), 377–392. https://doi.org/10.5194/angeo-29-377-2011

Prikryl, P., Jayachandran, P. T., Mushini, S. C., Pokhotelov, D., MacDougall, J. W., Donovan, E., et al. (2010). GPS TEC, scintillation and cycle slips observed at high latitudes during solar minimum. *Annales de Geophysique*, *28*(6), 1307–1316. https://doi.org/10.5194/angeo-28-1307-2010

Prikryl, P., Jayachandran, P. T., Mushini, S. C., & Richardson, I. G. (2014). High-latitude GPS phase scintillation and cycle slips during high-speed solar wind streams and interplanetary coronal mass ejections: A superposed epoch analysis. *Earth, Planets and Space*, *66*(1), 62. https://doi.org/10.1186/1880-5981-66-62

Rodger, A. S., Moffett, R. J., & Quegan, S. (1992). The role of ion drift in the formation of ionisation troughs in the mid- and high-latitude ionosphere—A review. *Journal of Atmospheric and Solar - Terrestrial Physics*, *54*(1), 1–30. https://doi.org/10.1016/0021-9169(92)90082-V

Schunk, R. W., Raitt, W. J., & Banks, P. M. (1975). Effect of electric fields on the daytime high-latitude E and F regions. *Journal of Geophysical Research*, *80*(22), 3121–3130. https://doi.org/10.1029/JA080i022p03121

Smith, A. M., Mitchell, C. N., Watson, R. J., Meggs, R. W., Kintner, P. M., Kauristie, K., & Honary, F. (2008). GPS scintillation in the high arctic associated with an auroral arc. *Space Weather*, *6*, S03D01. https://doi.org/10.1029/2007SW000349

Spogli, L., Alfonsi, L., De Franceschi, G., Romano, V., Aquino, M. H. O., & Dodson, A. (2009). Climatology of GPS ionospheric scintillations over high and mid latitude European regions. *Annales de Geophysique*, *27*(9), 3429–3437. https://doi.org/10.5194/angeo-27-3429-2009

St.-Maurice, J.-P., & Hanson, W. B. (1982). Ion frictional heating at high latitudes and its possible use for an in situ determination of neutral thermospheric winds and temperatures. *Journal of Geophysical Research*, *87*(A9), 7580–7602. https://doi.org/10.1029/JA087iA09p07580

van der Meeren, C., Oksavik, K., Lorentzen, D., Moen, J. I., & Romano, V. (2014). GPS scintillation and irregularities at the front of an ionization tongue in the nightside polar ionosphere. *Journal of Geophysical Research: Space Physics*, *119*, 8624–8636. https://doi.org/10.1002/2014JA020114

van der Meeren, C., Oksavik, K., Lorentzen, D. A., Paxton, L. J., & Clausen, L. B. N. (2016). Scintillation and irregularities from the nightside part of a Sun-aligned polar cap arc. *Journal of Geophysical Research: Space Physics*, *121*, 5723–5736. https://doi.org/10.1002/2016JA022708

van der Meeren, C., Oksavik, K., Lorentzen, D. A., Rietveld, M. T., & Clausen, L. B. N. (2015). Severe and localized GNSS scintillation at the poleward edge of the nightside auroral oval during intense substorm aurora. *Journal of Geophysical Research: Space Physics*, *120*, 10,607–10,621. https://doi.org/10.1002/2015JA021819

Van Dierendonck, A. J., Klobuchar, J., & Hua, Q. (1993). *Ionospheric scintillation monitoring using commercial single frequency C/A code receivers*. Paper presented at the 6th International Technical Meeting of the Satellite Division of The Institute of Navigation (ION GPS 1993), Salt Lake City, Utah, 22–24 Sept.

Wernik, A. W., Pożoga, M., Grzesiak, M., Rokicki, A., & Morawski, M. (2008). Monitoring ionospheric scintillations and TEC at the Polish Polar Station on Spitsbergen: Instrumentation and preliminary results. *Acta Geophysica*, *56*(4), 1129–1146. https://doi.org/10.2478/s11600-008-0060-8

Yeh, K. C., & Liu, C.-H. (1982). Radio wave scintillations in the ionosphere. *Proceedings of the IEEE*, *704*, 325–378.

Zou, S., Ridley, A., Jia, X., Boyd, E., Nicolls, M., Coster, A., et al. (2017). PFISR observation of intense ion upflow fluxes associated with an SED during the 1 June 2013 geomagnetic storm. *Journal of Geophysical Research: Space Physics*, *122*, 2589–2604. https://doi.org/10.1002/2016JA023697